

# The application of the generalized vector sample pattern matching method for EIT image reconstruction

Guoya Dong<sup>1,2</sup>, Richard H Bayford<sup>3,4</sup>, Shangkai Gao<sup>1</sup>, Yoshifuru Saito<sup>5</sup>,  
Rebecca Yerworth<sup>3,4</sup>, David Holder<sup>4</sup> and Weili Yan<sup>2</sup>

<sup>1</sup> Institute of Biomedical Engineering, Tsinghua University, Beijing, 100084,  
People's Republic of China

<sup>2</sup> Department of Electrical Engineering, Hebei University of Technology, Tianjin, 300130,  
People's Republic of China

<sup>3</sup> Middlesex University, Archway Campus, Furnival Building, Highgate Hill,  
London N19 3UA, UK

<sup>4</sup> Department of Clinical Neurophysiology, Middlesex Hospital, Cleveland Street,  
London W1T 8AA, UK

<sup>5</sup> Graduate School of Engineering, Hosei University, 3-7-2 Kajino, Koganei,  
Tokyo 184-8584, Japan

E-mail: dgy99@mails.tsinghua.edu.cn

Received 28 September 2002, in final form 7 March 2003

Published 30 April 2003

Online at [stacks.iop.org/PM/24/449](http://stacks.iop.org/PM/24/449)

## Abstract

This paper presents a new application of a generalized vector sample pattern matching (GVSPM) method for image reconstruction of conductivity changes in electrical impedance tomography. GVSPM is an iterative method for linear inverse problems. The key concept of the GVSPM is that the objective function is defined in terms of an angular component between the inner product of the known vector and solution of a system of equations. Comparisons are presented between images of simulated and experimental data, reconstructed using truncated singular value decomposition and GVSPM. In both cases, a normalized sensitivity matrix is constructed using the finite volume method to solve the forward problem.

Keywords: electrical impedance tomography (EIT), generalized vector sample pattern matching (GVSPM) method, finite volume method (FVM)

## 1. Introduction

The principal purpose of electrical impedance tomography (EIT) is to obtain the internal conductivity distribution of a bounded region by measuring the surface voltages when currents are injected into the target region. The advantages of EIT are that the technique is inexpensive,

portable and safe. It has been demonstrated that real-time images can be obtained at the rate of 25 images per second using the Sheffield Mk3.5 system (Wilson *et al* 2001). Thus, it has the potential for widespread use in medicine for continuous monitoring at the bedside, in the intensive care unit or in remote medical facilities. Its accuracy has been demonstrated in imaging lung (Metherall *et al* 1996) and brain function (Tidswell *et al* 2001a, 2001b).

The reconstruction of conductivity change images with EIT can be considered as a two-step process. First is the forward problem, which estimates the potential distribution using an assumed initial conductivity distribution, for a known current injected at the boundary. The second is the inverse problem, which reconstructs the internal conductivity changes given the potential distribution at the boundary. A number of researchers have used analytical and numerical solutions for the EIT forward problem (Liston *et al* 2002, Kleinermann *et al* 1997). Unfortunately, solutions for analytical methods are only available for simple geometries at present. Although numerical methods such as the finite element method (FEM) and finite difference method (FDM) can be used for complex geometries, they do not satisfy continuity conditions of both the normal component of the current density and the tangential component of the electrical field at the interfaces. A method which overcomes this drawback is known as the finite volume method (FVM). To improve the estimate of the reconstructed image, we have incorporated FVM into our reconstruction procedure.

The main purpose of this paper is to introduce a new application of the generalized vector sample pattern matching (GVSPM) (Endo *et al* 2002) method for image reconstruction of conductivity changes in EIT. We also demonstrate that FVM can be used to solve EIT forward problems by comparing its result with the analytical solution for a 2D model. It is shown that accurate estimates of the potential distribution can be obtained even with an FVM solution that uses a limited number of elements as compared to an equivalent FEM mesh.

The approach presented in this paper is a sensitivity method (Murai and Kagawa 1885, Metherall *et al* 1996, Gibson 2000) for the reconstruction of the conductivity changes. The sensitivity matrix is obtained from the solution of the EIT forward problem based on FVM. The GVSPM method, which is a powerful iterative solver, is then employed to solve the inverse problem.

The key concept of the GVSPM is that the objective function is defined in terms of an angular component between the inner product of the known vector and solution of a system of equations. As there is no accepted 'gold standard' to assess the quality of the GVSPM method, a comparison is made with the pseudo-inverse method based on the truncated singular value decomposition (TSVD) (Gibson 2000). The highest quality reconstructed images from both methods are used to evaluate the performance of GVSPM algorithm. Results are presented with both simulated and experimental data.

## 2. Method

### 2.1. FVM for EIT forward problem

FVM is one of the numerical methodologies in computational fluid dynamic problems. It was first introduced in 1994 to solve the volume conductor equation in bioelectrical studies of a concentric spherical model of the human head for investigating the influence of skull thickness on the scalp potential distribution (Abboud *et al* 1994). Since then, FVM has been applied to a large variety of bioelectric problems, e.g., the electrical activity of the heart in the torso or the fetus heart in the abdomen, and electrical activity in the human head (Eshel and Levy 1995, Rosenfeld and Tanami 1996).

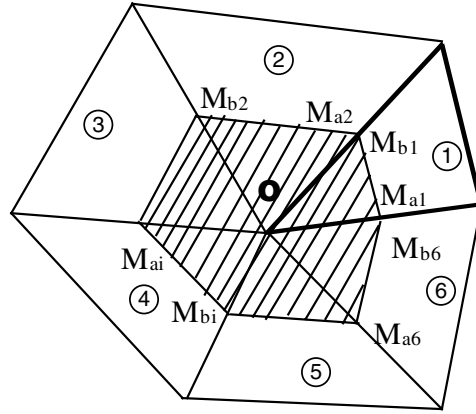


**Figure 1.** Generation of the primary and secondary cells in the 2D case. Six triangular primary cells and a secondary cell (shaded region), enclosing the common node O, are shown.

**2.1.1. Governing equation of FVM.** FVM is based on the current flow conservation law, which corresponds to the Kirchhoff current law (KCL) equation in circuit theory, i.e., the surface integral of the potential gradient in the presence of current sources in a control volume  $V$  with boundary surface  $S$  is given by the Gauss theorem,

$$\oiint_S (-\sigma \nabla \varphi) \cdot d\vec{S} = \iiint_V I_v dV \quad (1)$$

where  $\sigma$ ,  $\varphi$  and  $I_v$  are the conductivity, potential and current volume source density in the control volume, respectively. In EIT, there is no current volume source  $I_v$  assumed in the bounded region. Thereby, (1) reduces to

$$\oiint_S (-\sigma \nabla \varphi) \cdot d\vec{S} = 0. \quad (2)$$

with the following boundary conditions:

$$\begin{cases} -\sigma \frac{\partial \varphi}{\partial n} = J_n & \text{at the points where current is injected through the boundary } S \\ \sigma \frac{\partial \varphi}{\partial n} = 0 & \text{at the other points on } S \end{cases}$$

where  $J_n$  is the outward facing normal component of the current density.

**2.1.2. Discretization of the target volume.** To apply FVM to (2), the volume under investigation should be discretized first. In this paper, the target region is divided into a large number of triangular elements in 2D and tetrahedral elements in 3D. These elements are known as the primary cells in FVM, and are the same as the elements used in FEM. The difference between FEM and FVM is that, besides primary cells, there are secondary cells, which are also known as complementary cells in FVM. Because there is assumed to be no current source in the bounded region in EIT, the secondary cells are constructed by enclosing each of the nodes of the primary cells with a line joining the centre points of the edges sharing that node. The current fluxes across these surfaces are then calculated.

Figure 1 illustrates the primary and secondary elements for the 2D case. The node O is common to six triangular primary cells as shown, and  $M_{ai}$ ,  $M_{bi}$ ,  $i = 1, 2, \dots, 6$ , are the centre points of the edges sharing the common node O. Connecting these centre points leads to the

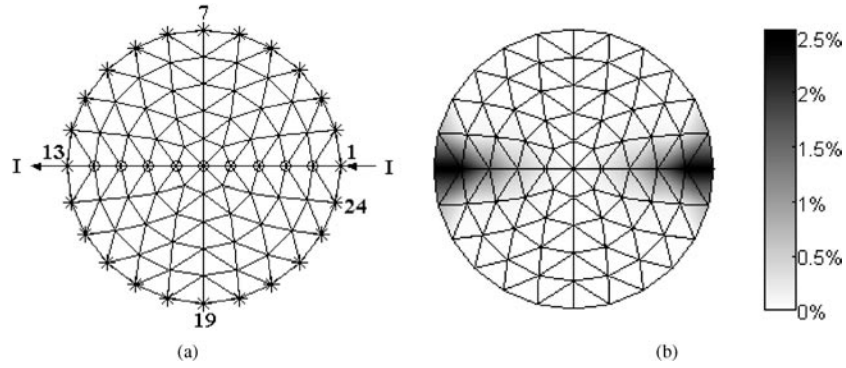


**Figure 2.** (a) A 2D coarse mesh system of 81 nodes and 136 elements. (b) The distribution of relative errors at nodes.

secondary cells enclosing the node O, shown by the shaded region. In each of the secondary cells, (2) reduces to a discretized form as follows.

For node O,

$$\sum_i \int_{l_i} (-\sigma \nabla \varphi) \cdot d\vec{l}_i = 0 \quad (3)$$

where  $i$  refers to the  $i$ th side of the secondary cell enclosing node O and  $l_i$  is the integration variable along this side.

In 3D cases, primary cells are tetrahedrons and secondary cells are constructed in a similar way to those of 2D (Dong *et al* 2002) and (2) reduces to a discretized form as follows:

$$\sum_i \int_{S_i} (-\sigma \nabla \varphi) \cdot d\vec{S}_i = 0 \quad (4)$$

where  $i$  refers to the  $i$ th surface of the secondary cell enclosing node O and  $S_i$  is the boundary of this surface. Comparing other discretization methods, such as hexahedron primary elements (Rosenfeld and Tanami 1996) and pentahedron primary elements (Xie *et al* 2001), with this method, reveals that the main advantages of our discretization method for generating the primary and secondary cells are (1) geometrical singularity is removed, (2) the coefficient matrix is sparse and symmetrical and (3) the calculation of the current flux can be carried out with higher accuracy.

**2.1.3. Validity of FVM solutions.** To verify the validity of the FVM solution, we compare the EIT forward problem results from the FVM method with an analytical solution for the 2D homogeneous circular model (Dong *et al* 2002). A 2D triangular coarse mesh system with 81 nodes and 136 primary elements is adopted and shown in figure 2(a). The current is injected diametrically through the driving pair at nodes 1–13. Boundary nodes are numbered from 1 to 24. Inner nodes along the axis of current injection are marked with small circles. In order to access the accuracy of FVM results using the analytical solution as a reference, the relative error  $e_r$  is defined as

$$e_r = \frac{|\varphi_{\text{FVM}} - \varphi_{\text{ana}}|}{|\varphi_{\text{ana\_max}} - \varphi_{\text{ana\_min}}|} \times 100\% \quad (5)$$

where  $\varphi_{\text{FVM}}$  is the potential solution by FVM and  $\varphi_{\text{ana}}$  is the analytical solution.  $\varphi_{\text{ana\_max}}$  and  $\varphi_{\text{ana\_min}}$  are the maximal and minimal potentials, respectively, of the analytical solution

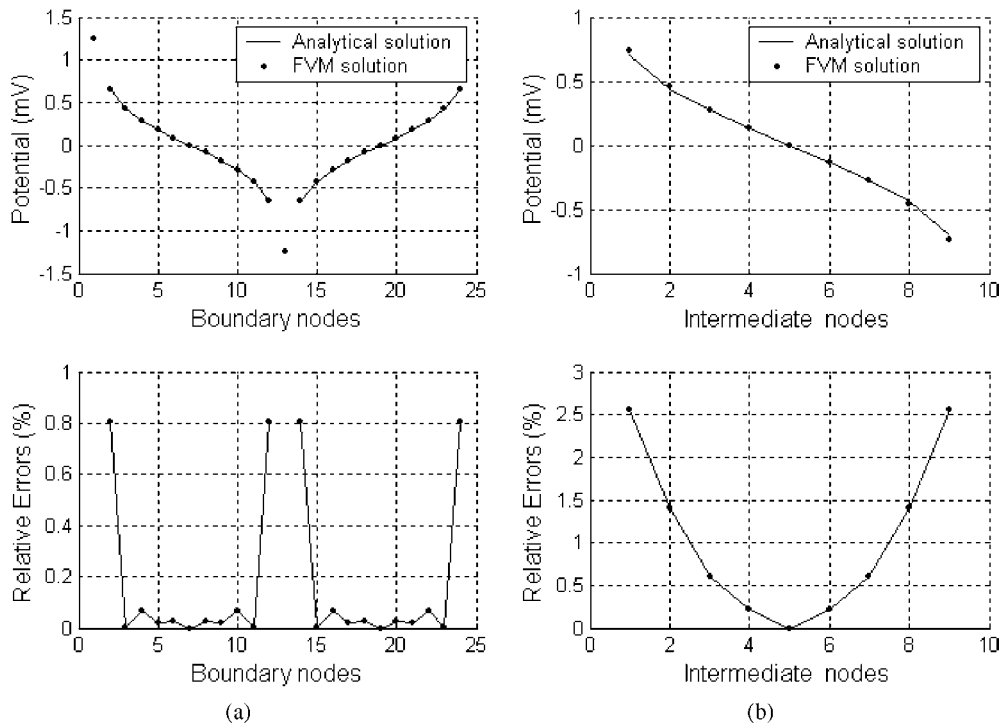


**Figure 3.** Comparisons between the FVM solution and analytical solution for the EIT forward problem. The upper row illustrates the potential distribution and the lower row the relative errors. (a) Boundary nodes. (b) Intermediate nodes along the axis between the current injection electrodes.

among all nodes except the two nodes through which the current is injected because these two nodes are singular points for the analytical solution, and therefore have infinite potentials.

Figure 2(b) shows the relative error distribution at each node. Figure 3 shows the comparison of both potential values and relative errors between analytical and FVM solutions. Figure 3(a) shows the comparison at the boundary nodes and figure 3(b) shows the comparison at intermediate nodes along the axis of current injection from right to left. Figures in the upper row are the calculated potentials while those in the lower row are the relative errors.

From these results, we can see that the relative errors are within 0.3% at most of the nodes. The larger relative errors, up to 2.56%, are distributed around the drive pair, nodes 1 and 13, and along the axis joining them. Thus, accurate estimates of the potential distribution can be obtained even with an FVM solution that uses a coarse mesh.

## 2.2. Construction of system matrix

The normalized sensitivity matrix method (Metherall *et al* 1996) is used for EIT reconstruction in this paper. The sensitivity matrix  $S$  and each individual boundary voltage measurement vector  $\Delta V$  are normalized by the uniform boundary voltage vector before inversion in order to prevent instability from measurement errors, such as in placement of electrodes and the configuration of electrode pairs in clinical studies (Metherall *et al* 1996). Therefore, the normalized sensitivity matrix  $F$  describes the normalized linear sensitivity relationship between

normalized changes in the boundary voltages  $\Delta V_n$  and normalized changes in conductivity  $\Delta\sigma_n$  as

$$\Delta V_n = F \cdot \Delta\sigma_n. \quad (6)$$

Simulated data  $\Delta V_{sim}$  were constructed by subtracting the boundary voltage vector generated from a uniform conductivity distribution from that generated in a non-uniform conductivity distribution, instead of by multiplying a vector of conductivity changes  $\Delta\sigma$  by the normalized sensitivity matrix  $F$  (Liston *et al* 2002).

### 2.3. Image reconstruction

The EIT reconstruction problem is in essence reduced to solving the ill-posed system of (6). In the early 1990s, a strategy called the sample pattern matching (SPM) method was proposed for solving ill-posed linear systems of equations. The principle is to search for the patterns represented by the column vectors in order to satisfy the known vector. It has been used for source position searching of the human eye field (Saito *et al* 1990), crack identification in metallic materials (Saotome *et al* 1993), shape design of magnetic cores (Saotome *et al* 1995) and so on. The generalized solver, generalized sample pattern matching (GSPM) method has been applied to dose optimization of electron beams (Saito and Yoda 1996, Yoda *et al* 1997) and so on. The GVSPM method is the improved method in which the objective function is the angle between the normalized known vector and the normalized solution of a system of equations (Endo *et al* 2002).

In this paper, we apply GVSPM for searching the conductivity changes in EIT. If we represent the measured surface voltage vector  $\Delta V_n$  by  $\mathbf{Y}$  of dimension  $n$ , the solution vector of conductivity changes  $\Delta\sigma_n$  by  $\mathbf{X}$  of dimension  $m$ , and the normalized sensitivity matrix  $F$  by  $C$  which is an  $n \times m$  rectangular matrix, equation (6) can be written as

$$\mathbf{Y} = C\mathbf{X}. \quad (7)$$

Equation (7) could be rewritten as

$$\mathbf{Y} = \sum_{i=1}^m x_i \mathbf{C}_i \quad \mathbf{X} = [x_1 \quad x_2 \quad \cdots \quad x_m]^T \quad C = [\mathbf{C}_1 \quad \mathbf{C}_2 \quad \cdots \quad \mathbf{C}_m]. \quad (8)$$

Equation (8) means that the known vector  $\mathbf{Y}$  is represented by means of a linear combination of column vectors  $\mathbf{C}_i$ ,  $i = 1, 2, \dots, m$ , in the system matrix  $C$ .

GVSPM is an iterative algorithm. The key idea is that the angle between the known vector  $\mathbf{Y}$  and vector  $C\mathbf{X}^{(k)}$  (superscript  $k$  stands for the index of iteration) should approach zero when the solution  $\mathbf{X}$  is reached. In other words, the solution  $\mathbf{X}$  would be obtained when the inner product between the normalized  $\mathbf{Y}$  and normalized  $C\mathbf{X}^{(k)}$  reaches 1:

$$\frac{\mathbf{Y}}{|\mathbf{Y}|} \cdot \frac{C\mathbf{X}^{(k)}}{|C\mathbf{X}^{(k)}|} \rightarrow 1. \quad (9)$$

Therefore, normalization of the known vector by vector 2-norm  $|\mathbf{Y}|$  is necessary as

$$\frac{\mathbf{Y}}{|\mathbf{Y}|} = \sum_{i=1}^m x_i \frac{|\mathbf{C}_i|}{|\mathbf{Y}|} \frac{\mathbf{C}_i}{|\mathbf{C}_i|} \quad \text{or} \quad \mathbf{Y}' = C'\mathbf{X}'. \quad (10)$$

$$C' = [C'_1, C'_2, \dots, C'_m] = \left[ \frac{\mathbf{C}_1}{|\mathbf{C}_1|}, \frac{\mathbf{C}_2}{|\mathbf{C}_2|}, \dots, \frac{\mathbf{C}_m}{|\mathbf{C}_m|} \right] \quad (11)$$

$$\mathbf{X}' = [x'_1, x'_2, \dots, x'_m]^T = \left[ x_1 \frac{|\mathbf{C}_1|}{|\mathbf{Y}|}, x_2 \frac{|\mathbf{C}_2|}{|\mathbf{Y}|}, \dots, x_m \frac{|\mathbf{C}_m|}{|\mathbf{Y}|} \right]^T$$

where the prime ( $'$ ) denotes the normalized quantities.

Equation (9) could then be rewritten as

$$\mathbf{Y}' \cdot \frac{C' \mathbf{X}'^{(k)}}{|C' \mathbf{X}'^{(k)}|} \rightarrow 1. \quad (12)$$

The normalized vector  $\mathbf{Y}'$  could be considered as a vector with unit amplitude in an  $m$ -dimensional space spanned by the vectors  $C'_1, C'_2, \dots, C'_m$  and scalars  $x'_1, x'_2, \dots, x'_m$  are their corresponding weighting coefficients, which can be calculated by the 'parallelogram rule' (Berberian 1992). If the coordinate system is orthogonal, then the weights are the orthogonal projections of the vector  $\mathbf{Y}$  in the coordinate directions which can be found by the inner product:

$$\begin{bmatrix} x'_1 \\ x'_2 \\ \dots \\ x'_m \end{bmatrix} = \begin{bmatrix} C'_1 \cdot \mathbf{Y}' \\ C'_2 \cdot \mathbf{Y}' \\ \dots \\ C'_m \cdot \mathbf{Y}' \end{bmatrix} \quad \text{or} \quad \mathbf{X}' = C'^T \mathbf{Y}'. \quad (13)$$

However, in the present case, the normalized column vectors  $C'_1, C'_2, \dots, C'_m$  are not orthogonal so that weights are not equal to the orthogonal projections. Usually, it is difficult to get the weights for a non-orthogonal coordinate system with the 'parallelogram rule'.

The GVSPM just employs the orthogonal projections to approximate the weights in coordinate directions  $C'_1, C'_2, \dots, C'_m$  and then finds the final solution in an iterative way. The iteration follows the steps:

- (1) *Initialization*. Set the initial solution vector  $\mathbf{X}'^{(0)}$  to be the orthogonal projections of the known normalized vector  $\mathbf{Y}'$  in the coordinate direction.

$$\mathbf{X}'^{(0)} = C'^T \mathbf{Y}' \quad (14)$$

- (2) *Iteration*

(i) Set  $k = 0$ .

- (ii) The initial estimated vector  $Y^{(k)}$  is obtained as

$$\mathbf{Y}^{(k)} = C' \mathbf{X}'^{(k)}. \quad (15)$$

- (iii) Normalize  $Y^{(k)}$ :

$$\mathbf{Y}'^{(k)} = \frac{\mathbf{Y}^{(k)}}{|\mathbf{Y}^{(k)}|}.$$

- (iv) Find the deviation vector:

$$\Delta \mathbf{Y}'^{(k)} = \mathbf{Y}' - \mathbf{Y}'^{(k)}. \quad (16)$$

$\Delta \mathbf{Y}'^{(k)}$  reflects the angle between  $\mathbf{Y}'$  and  $\mathbf{Y}'^{(k)}$  and the direction in which  $\mathbf{Y}'^{(k)}$  should be rotated towards  $\mathbf{Y}'$ .

- (v) Update:

$$\mathbf{X}'^{(k+1)} = \mathbf{X}'^{(k)} + C'^T \Delta \mathbf{Y}'^{(k)}. \quad (17)$$

- (vi) Increase  $k$  to  $k + 1$ , go back to (ii).

A simple but intuitive explanation of the process is given in the appendix.

### 3. Results

In the 2D case a physical model, a circle with a radius of 92 mm, was used for the target volume. It was meshed using 596 nodes and 1110 elements (figure 3(a)). Ninety-six pairs of measurement were obtained with a diametric current injection and adjacent voltage measurement ('opposite-adjacent pattern'). The number of measurements was chosen to be the same as the number provided by the data collection system (Yerworth *et al* 2002). In this section, images of conductivity changes reconstructed by both the GVSPM and pseudo-inverse (PINV routine in Matlab6.1, The Mathworks, Inc.) methods are shown for comparison.

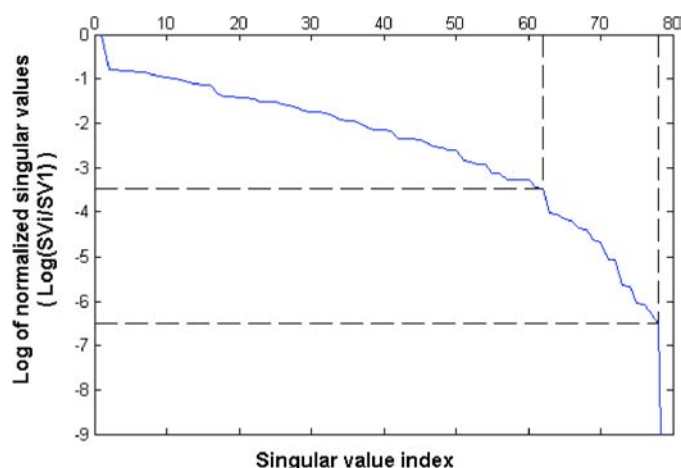


**Figure 4.** Plot of log of singular values from the circular normalized sensitivity matrix. The left vertical dashed line corresponds to the singular value index of 62. The right one corresponds to the singular value index of 78.

### 3.1. Reconstruction of 2D simulated data

Pseudo-inverse is a method based on truncated singular value decomposition (TSVD) while the GVSPM is an iterative method. In this paper, the choices of the truncation level for the pseudo-inverse method and the convergence threshold for the GVSPM method are both based on the quality of the reconstructed image. Figure 4 illustrates the singular value spectrum where the steep descent points are at 62 and 78 singular values. In order to compare the quality of the image under different situations, a perturbation with conductivity change of 30% is defined in a small region containing six elements with a radius of about 6 mm, located at 30 mm from the centre of the circle, as shown in figure 5(a). For the pseudo-inverse method, the images are reconstructed at three different truncation levels which include 50, 62, 78 singular values, respectively, as shown in figures 5(d)–(f). Although the resolution of the image with 78 singular values is the best, a symmetrically located artefact image of opposite conductivity changes is created as well. With the decrease in the truncation level to 50 singular values, the image becomes smoother but the resolution becomes lower. Therefore, for the pseudo-inverse method, the truncation level is set to 62 singular values for simulated data free from noise. Of course, it is possible to improve the quality of the TSVD if better regularization is incorporated, but the aim is to use this as a comparison method and not to compare which is the best implementation of TSVD.

For the GVSPM method, the threshold for the cosine of the angle between the known vector and the vector  $C\mathbf{X}^{(k)}$  of system equations is chosen not only on the basis of the quality of the image but also on the computation time. Figures 5(b) and (c) are the reconstructed images by the GVSPM method with the thresholds of 0.99995 and 0.99999, respectively. The image resolution in figure 5(c) has not improved much compared to figure 5(b), hence the threshold is set to 0.99995 in order to minimize the computation requirements.

**3.1.1. Performance for single perturbation.** In this case, conductivity changes of 30% are defined in a small region containing six elements with a radius of about 6 mm, moving from the boundary to the centre of the circle. Figure 6(a) shows the original conductivity distribution when the perturbation is located 44 mm from the centre of the circle. As shown in figure 6,

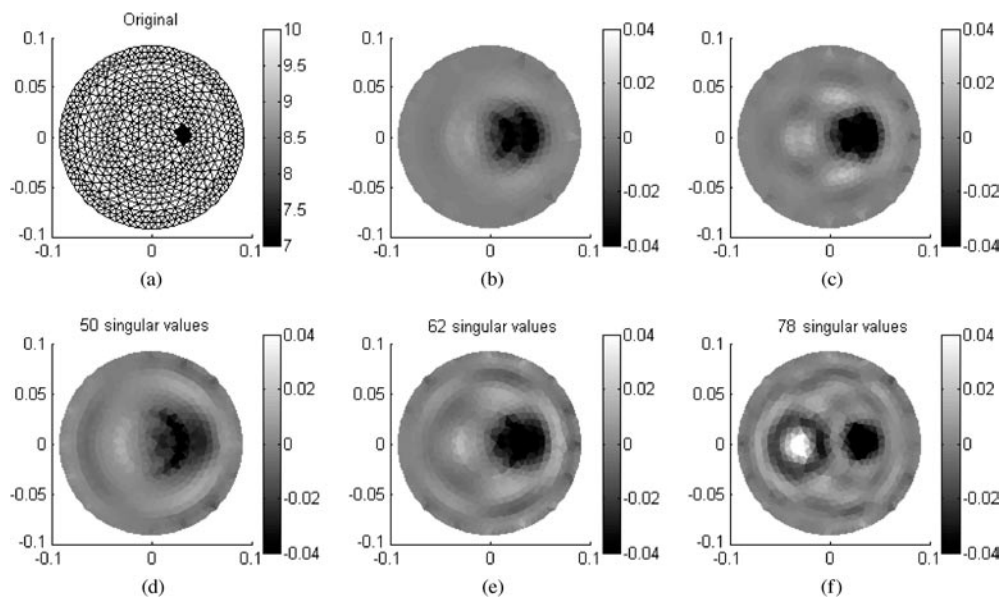


**Figure 5.** The comparison of images reconstructed with different truncation levels and thresholds for the pseudo-inverse and GVSPM methods, respectively. (a) Original conductivity distribution. (b), (c) GVSPM results with thresholds of 0.99995 and 0.99999, respectively. (d)–(f) Pseudo-inverse results with the truncation levels at 50, 62 and 78 singular values.

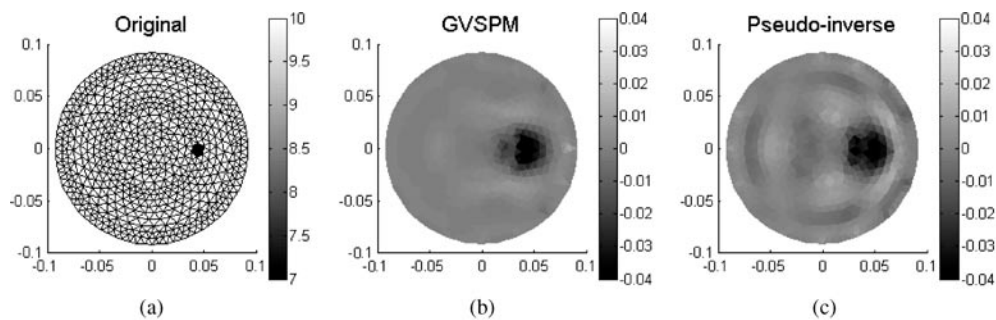


**Figure 6.** Results for single perturbation with conductivity change of 30% located 44 mm apart from the centre of the circle. (a) Original conductivity distribution. (b) GVSPM result. (c) Pseudo-inverse result with truncation to 62 singular values.

comparing the GVSPM result with the pseudo-inverse result, we can see that the image reconstructed by GVSPM is more reliable and smoother. The localization error is within 2.5 mm when the distance between the perturbed region and the centre of the circle is over 30 mm. When the perturbed region moves to within 10 mm of the centre, both the images by the GVSPM and pseudo-inverse methods perform worse than for longer distances (figure 7).

**3.1.2. Distinguishability with two perturbations.** Two cases are used in this section to check the distinguishability with two perturbations. In the first case, there are two small regions with radii of about 6 mm located symmetrically with respect to the centre of the circle, having the

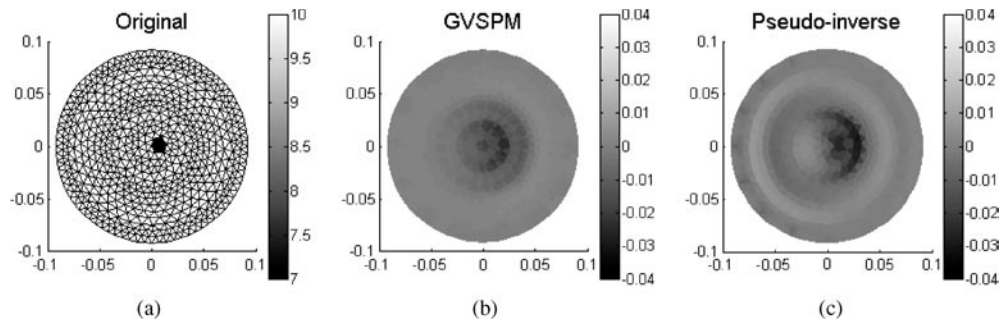


**Figure 7.** Comparison with the perturbation located 5 mm from the centre of the circle. (a) Original conductivity distribution. (b) GVSPM result. (c) Pseudo-inverse result.

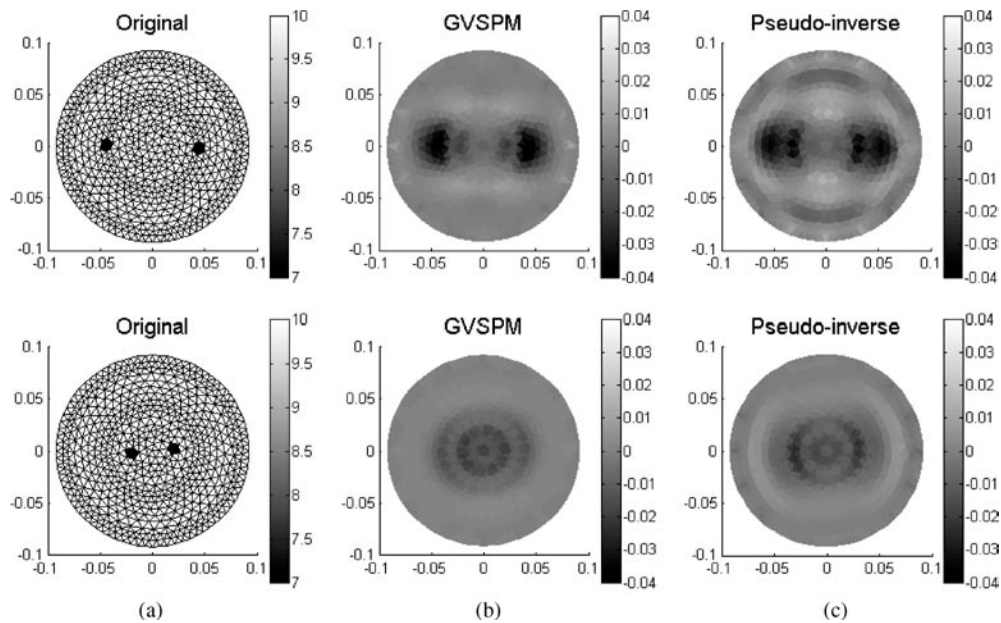


**Figure 8.** Results with two identical conductivity changes of 30%, moving towards the centre. (a) Original conductivity distribution. (b) GVSPM results. (c) Pseudo-inverse results.

same conductivity changes of 30%. They are gradually moved towards the centre, along the  $x$ -axis of the circle. In the second case, opposite conductivity changes of  $\pm 30\%$  are defined in the two small regions and moved in the same way as the first case. For the former case (figure 8), the images obtained by both GVSPM and pseudo-inverse methods perform better towards the edge than the centre. When their centres are less than 20 mm from the centre of the circle, the images are too blurred to distinguish them. However, for the latter case (figure 9), the images obtained by both methods are of high enough resolution for the changes to be distinguishable, even when their centres are less than 10 mm from the centre of the circle, as shown in the second row of figure 9. Furthermore, comparing the results of the GVSPM and pseudo-inverse methods, we can see that the image quality is better with GVSPM.

By combining FVM, for the EIT forward problem, with a normalized sensitivity matrix method, for the EIT reconstruction, a conductivity change as small as 1% can be distinguished

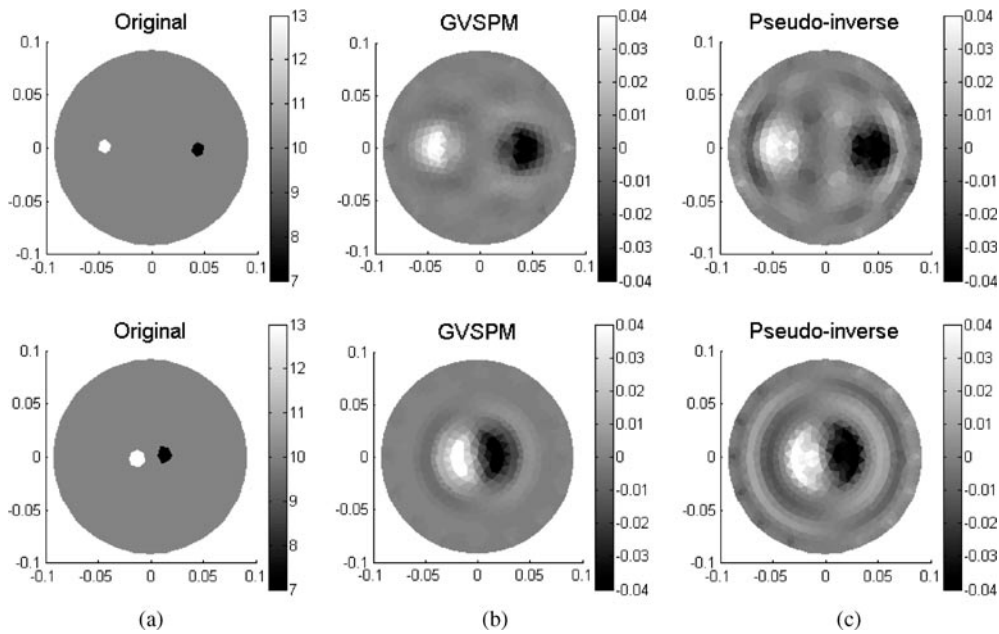


**Figure 9.** Results with two opposite conductivity changes of 30%, moving towards the centre. (a) Original conductivity distribution. (b) GVSPM results. (c) Pseudo-inverse results.

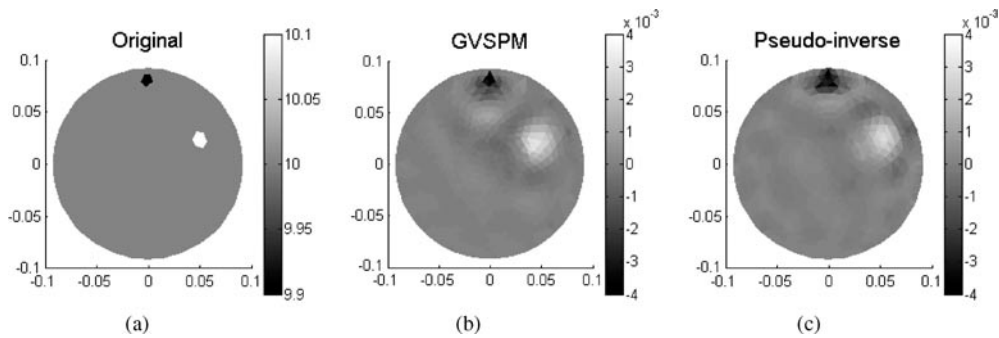


**Figure 10.** Results with a change as small as 1%. (a) Original conductivity distribution. (b) GVSPM result. (c) Pseudo-inverse result.

by both pseudo-inverse and GVSPM methods (figure 10). In this case, conductivity changes of  $\pm 1\%$  are defined in two regions (figure 10(a)). From the results, we can see that a higher image quality is obtained by using GVSPM.

Finally, we show an example with four perturbations (figure 11). Conductivity changes of  $-30\%$  are defined in two regions located towards the top and bottom of the circle, and the other two perturbations with conductivity changes of  $30\%$  are defined in two regions located to the left and right sides of the circle, respectively.

### 3.2. Reconstruction of 2D experimental data

The 2D tank was made from a circular Perspex pan with a radius of 92 mm, depth 20 mm. Sixteen electrodes were uniformly arranged around the circular surface. Ninety-six pairs of

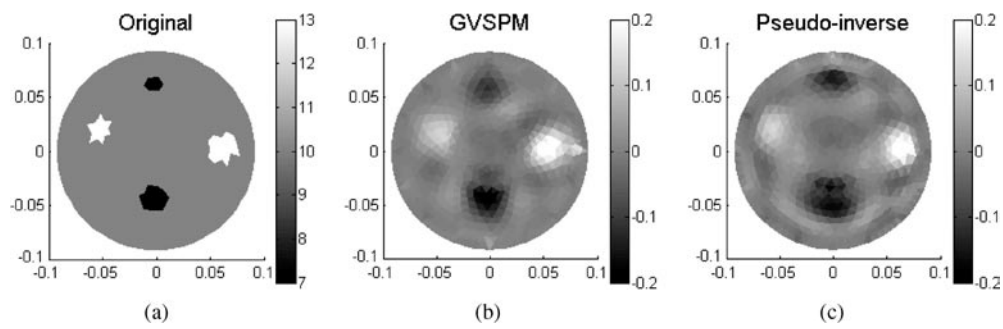


**Figure 11.** The results with four perturbations. (a) Original conductivity distribution. (b) GVSPM result. (c) Pseudo-inverse result.

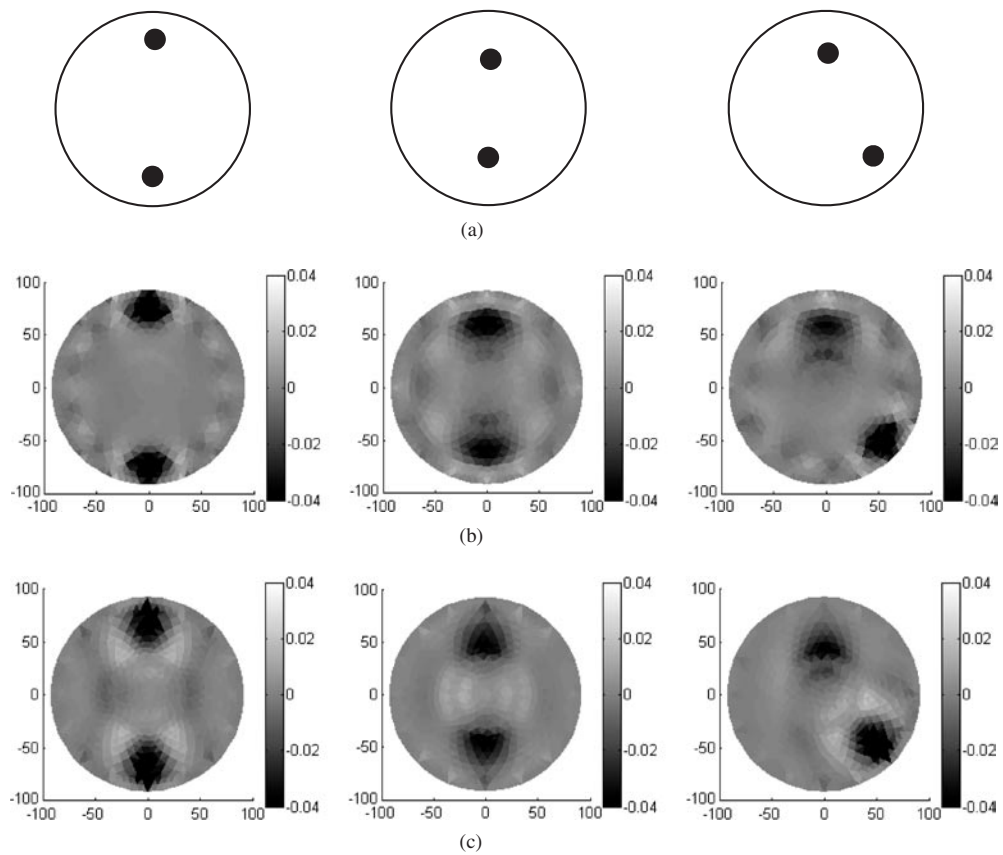


**Figure 12.** Reconstruction results with two Perspex objects. (a) The original positions of the Perspex objects. (b) Pseudo-inverse results. (c) GVSPM results.

measurements were carried out with the opposite-adjacent pattern. The tank was filled with 0.2% saline. The object put into the saline is a cylinder made from Perspex with a radius of 10 mm, and a height of 20 mm. The noise level of the measurement system is about 0.25%. Therefore, for the experimental data, the truncation level for the pseudo-inverse method is

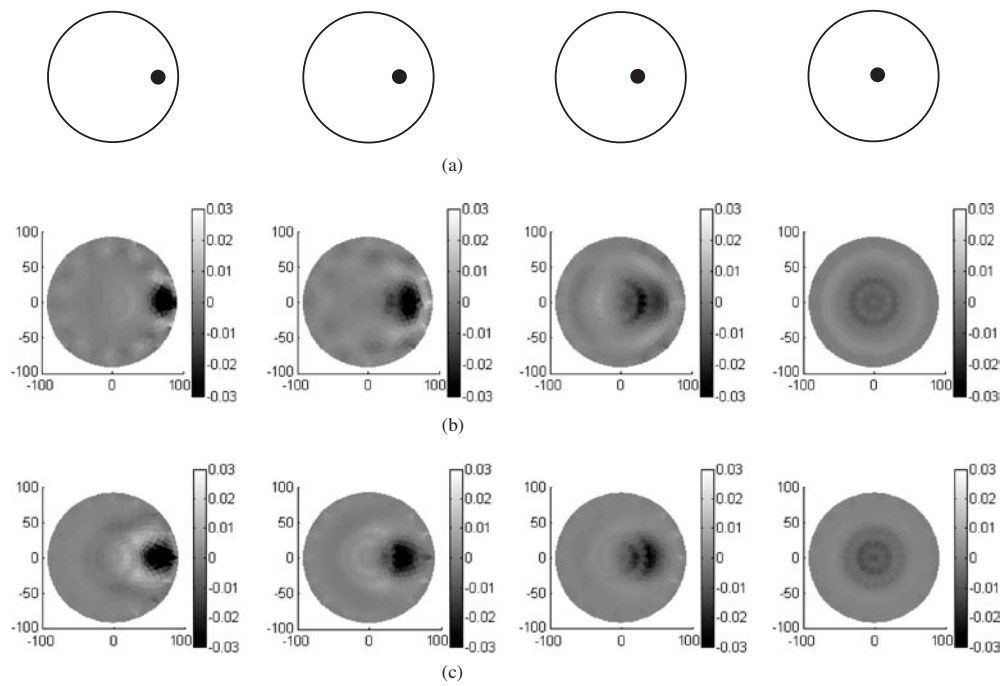


**Figure 13.** The reconstruction results with one Perspex object moving from the left side to the centre of the saline. (a) The original positions of the Perspex object. (b) Pseudo-inverse results. (c) GVSPM results.

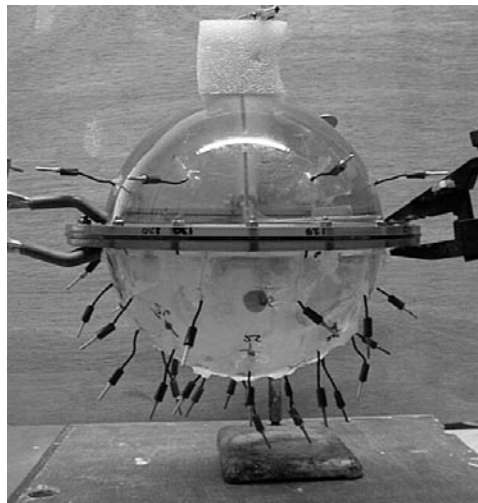


**Figure 14.** Picture of the spherical tank.

set to 50 singular values corresponding to a value of about 0.25% relative to the maximum singular value of system matrix. For the GVSPM, the threshold is set to 0.99995 as before.

Figure 12 shows the results for two pieces of Perspex located at different positions. Figure 13 shows the results with one piece of Perspex moving gradually from the left to the

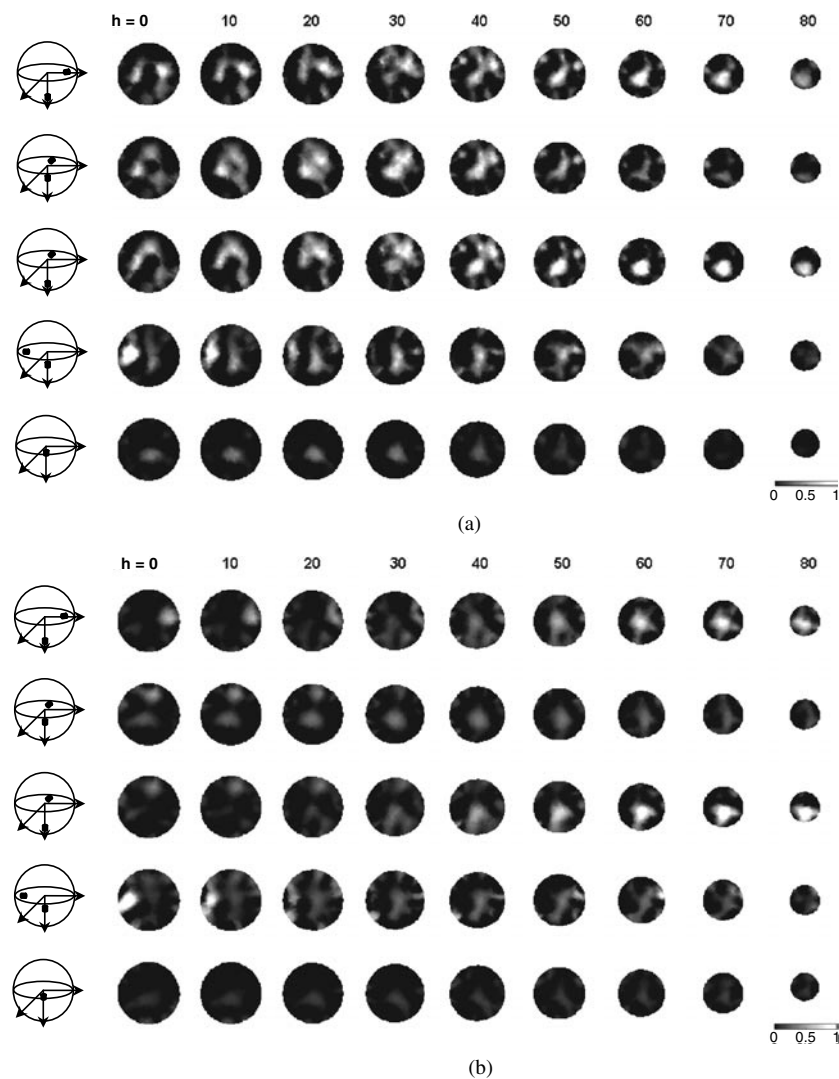


**Figure 15.** Reconstruction results of the 3D experimental tank. (a) GVSPM results. (b) Pseudo-inverse results.

centre of the circle. From the results we can see that the reconstructed images with GVSPM have less artefact error. This performance is the same as for the images reconstructed with noiseless simulated data.

For the images reconstructed by GVSPM with 1.4 GHz CPU equipped with 1.5 Gbyte of RAM, when the threshold is set to 0.99995, the number of iterations for reconstructing the images is between 77 and 264, and the time required to complete the reconstruction is from 1.03 s to 3.4 s respectively.

### 3.3. Reconstruction of 3D experimental data

The 3D spherical tank (figure 14) was made from two Perspex bowls with 19 cm inner diameter. Thirty-one electrodes, made of chlorided silver balls 1 mm in diameter, were

inserted on the inner surface of the bowl in positions based on a modified 10–20 system of electroencephalography (EEG) electrode placement (Tidswell *et al* 2001a, 2001b).

The tank was filled with 0.2% saline. EIT data were acquired when impedance perturbations were generated by one or two pieces of cylindrical Perspex inserted inside the saline-filled tank. Each image consisted of 258 measurements made from different combinations of the 31 tank electrodes, using the opposite–adjacent pattern (Tidswell *et al* 2001a, 2001b).

The mesh generated for the spherical model consists of 18 131 tetrahedral primary elements and 3514 nodes. The truncation level for the pseudo-inverse method is set to 80 singular values for 3D experimental data, because of the 0.25% experimental noise. Because of the longer time needed for convergence with 3D, the threshold is set to 0.995 for GVSPM. With this threshold, the averaged number of iterations for image reconstruction is about 120.

The first four rows in figures 15(a) and (b) show the reconstructed images with two pieces of Perspex put in the tank, by the GVSPM and pseudo-inverse methods respectively. One piece of Perspex was located in the equatorial plane at  $3/4r$ , where  $r$  is the radius of the sphere, and rotated between images, as indicated in the first columns. The other was located on the  $-z$ -axis and moved between  $-3/4r$  and  $-1/4r$ . The fifth rows in figure 15(a) and (b) show the images with one piece of Perspex located on the  $-z$ -axis of  $-1/4r$ . Each row represents a different Perspex position. Each image is split into the same nine slices along the  $-z$ -axis. The first column shows the position of the Perspex located in the tank. The other columns are the  $x$ – $y$  plane from the reconstructed images, located  $h$  mm below the equator plane.

#### 4. Discussion and conclusion

This initial work demonstrates that the FVM provides an alternative method for solving the forward problem for simple 2D and 3D objects. However, it needs further investigation with a 3D shell model and comparing the results from FEM and BEM to demonstrate its accuracy. The comparison with the analytical solution for a model of a 2D homogenous circle shows accurate estimates of the potential distribution. By combining FVM with a normalized sensitivity matrix method, for the EIT reconstruction, a conductivity change as small as 1% can be distinguished.

The comparisons between the solutions from the GVSPM and pseudo-inverse methods yielded the following observations:

- (1) With the pseudo-inverse method, the position of the reconstructed perturbation tends to the boundary. The GVSPM method leads to more precise localization and the reconstructed images are improved.
- (2) The GVSPM method is more sensitive to a perturbation located in the central region (e.g., figure 9 in the 2D case, two opposite perturbations defined at the central region, and figure 12 in the 3D case, the fifth column, one piece of Perspex located near the central region). Moreover, the images by the GVSPM method are more focused than those by the pseudo-inverse method. This is because the pseudo-inverse method uses truncated SVD, in an attempt to stabilize the inversion process. This is unlike the GVSPM method uses the full data extent.
- (3) One difference between the 3D and 2D cases is that more artefacts are created by the GVSPM method in the 3D case, which may be caused by the same error in the electrode positions that lead to the slow convergence speed, especially after the cosine of the angle between the known vector and the  $k$ th solution vector of system equations is larger than 0.995. This point needs to be verified further by a better meshing system with electrodes

located exactly at a surface node. Another reason for this increased level of artefact error is the significantly higher ratio of number of mesh elements to number of boundary measurement in the 3D case. This makes the 3D problem much more underdetermined than the 2D.

In conclusion, GVSPM is shown to be a powerful iterative solver for the EIT reconstruction problem. It enables us to obtain reliable and stable solutions for image reconstructions of conductivity changes.

In the near future, the complete electrode model (Päivi and Vauhkonen 1999) will be adopted to improve the accuracy of the EIT forward problem at the nodes near the driving electrodes. Also the FVM and GVSPM methods will be employed in research on 3D multi-layer sphere and 3D real head models.

### Acknowledgments

This work was supported by NSFC no 59937160 and HBNSF no 501037, China. The authors would like to thank Professor Fusheng Yang, Professor Xinshan Ma and Professor Iliana Marinova for critical comments and Louis Enfield and Adam Liston for reading the manuscript.

### Appendix

We take a 2D system as an intuitive simple example to show the process of iteration and to depict the convergence process of the GVSPM method. Figure 16 shows a circle with unit radius.

- (1) The normalized vector  $\vec{Y}'$  is a vector with unit amplitude in a two-dimensional space spanned by the vectors  $\vec{C}'_1, \vec{C}'_2$  and scalars  $x'_1, x'_2$  are their corresponding weighting coefficients.
- (2) Set the initial solution vector  $\mathbf{X}^{(0)} = [x_1^{(0)}, x_2^{(0)}]^T$  to be the projections of the known normalized vector  $\vec{Y}'$  according to (14). And then the initial solution vector of system equations  $\vec{Y}^{(0)}$  is obtained by the ‘parallelogram rule’; the normalized vector is shown in figure 16 as

$$\vec{Y}^{(0)} = \vec{Y}^{(0)} / |\vec{Y}^{(0)}|. \quad (\text{A1})$$

It should be noted that the vector  $\vec{Y}^{(0)}$  shown in figure 16 is not the actual one. It is exaggerated so as to make the figure clearer. The actual vector should be closer to the vector  $\vec{Y}'$ .

- (3) The first deviation vector  $\Delta\vec{Y}^{(0)}$  is obtained by subtracting the normalized vector  $\vec{Y}^{(0)}$  from vector  $\vec{Y}'$  by ‘vector subtraction’, i.e.,

$$\Delta\vec{Y}^{(0)} = \vec{Y}' - \vec{Y}^{(0)}. \quad (\text{A2})$$

$\Delta\vec{Y}^{(0)}$  reflects the angle between the vector  $\vec{Y}'$  and  $\vec{Y}^{(0)}$  and the direction at which  $\vec{Y}^{(0)}$  should be rotated towards  $\vec{Y}'$ .

- (4) By orthogonally projecting  $\Delta\vec{Y}^{(0)}$  onto the coordinate directions  $\vec{C}'_1, \vec{C}'_2$ , projections  $\Delta\mathbf{X}^{(0)} = [\Delta x_{1\perp}^{(0)}, \Delta x_{2\perp}^{(0)}]^T$  are obtained respectively. Then, rotating  $\vec{Y}^{(0)}$  along the direction of the vector  $\Delta\vec{Y}^{(0)}$  according to the vector summation, the next estimated vector  $\vec{Y}^{(1)}$  is worked out. The corresponding weights of  $\vec{Y}^{(1)}$  are obtained as

$$\begin{aligned} \mathbf{X}^{(1)} &= \mathbf{X}^{(0)} + \mathbf{C}'^T \Delta\mathbf{X}^{(0)} \\ &= \mathbf{X}^{(0)} + \Delta\mathbf{X}^{(0)}. \end{aligned}$$

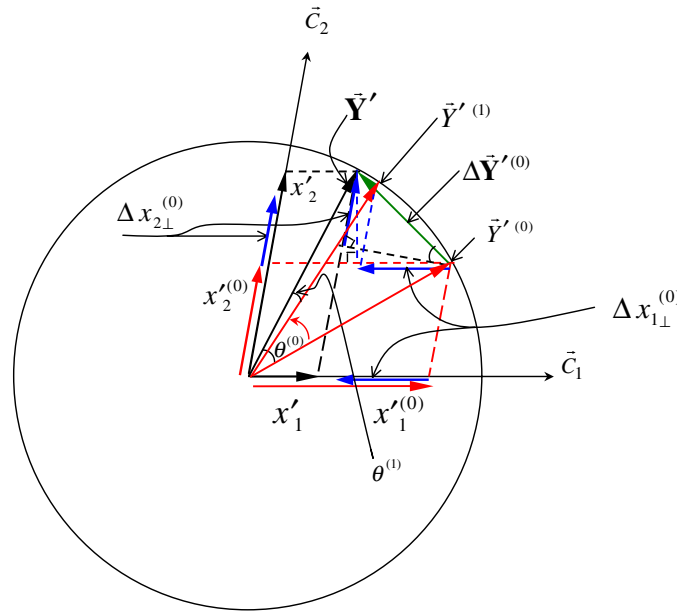


**Figure 16.** Illustrating the convergence process of the GVSPM method.

Normalize  $\vec{Y}^{(1)}$  to  $\vec{Y}'^{(1)}$  which is of unit amplitude in order to constrain the solution vector of the system equation to always rotate along the unit circle. Steps (3) and (4) show how the initial normalized vector  $\vec{Y}'^{(0)}$  tends to the next normalized vector  $\vec{Y}'^{(1)}$ .

- (5) Repeating steps (3) and (4), the convergence process continues until the angle between  $\vec{Y}'$  and  $\vec{Y}'^{(k)}$  reaches zero, i.e.,

$$\vec{Y}' \cdot \vec{Y}'^{(k)} \rightarrow 1. \quad (\text{A3})$$

## References

- Abdoud S *et al* 1994 Numerical calculation of the potential distribution due to dipole sources in a spherical model of the head *Comp. Biomed. Res.* **27** 441–55
- Berberian S K 1992 *Linear Algebra* (Oxford: Oxford Science Publications)
- Dong G, Ma X, Gao S, Xie Y and Saito Y 2002 Derivation from current density distribution to conductivities based on the adjoint field theory and numerical test with finite volume method *Proc. 2nd Japan, Australia and New Zealand Joint Seminar on Applications of Electromagnetic Phenomena in Electrical and Mechanical Systems (Kanazawa, Japan, Jan. 24–25)* pp 89–96
- Endo H, Hayano S, Saito Y and Miya K 2002 Generalized vector sampled pattern matching method—theory and applications *Electromagnetic Nondestructive Evaluation (VI) (Studies Appl. Electromagn. Mech. 23)* ed F Kojima (The Netherlands: IOS Press) pp 285–92
- Eshel Y and Levy S 1995 Correlation between skull thickness asymmetry and scalp potential estimated by a numerical model of the head *IEEE Trans. Biomed. Eng.* **42** 242–9
- Gibson A 2000 Electrical impedance tomography of human brain function *PhD Thesis* Department of Physiology, University College, London
- Kleinermann F *et al* 1997 Analytical solution to the forward problem for finite elliptic cylinder *World Congress on Medical Physics and Biomedical Engineering* **35** (suppl. part 1) 322
- Liston A, Bayford R H, Tidswell A T and Holder D S 2002 A multi-shell algorithm to reconstruct EIT images of brain function *Physiol. Meas.* **23** 105–19
- Metherall P, Barber D C, Smallwood R H and Brown B H 1996 Three dimensional electrical impedance tomography *Nature* **380** 509–12

- Murai T and Kagawa Y 1985 Electrical impedance computed tomography based on a finite element model *IEEE Trans. Biomed. Eng.* **32** 177–84
- Päivi J and Vauhkonen M 1999 Three-dimensional electrical impedance tomography based on the complete electrode model *IEEE Trans. Biomed. Eng.* **46** 1150–60
- Rosenfeld M and Tanami R 1996 Numerical solution of the potential due to dipole sources in volume conductors with arbitrary geometry and conductivity *IEEE Trans. Biomed. Eng.* **43** 679–89
- Saito Y, Itagaki E and Hayano S 1990 A formulation of the inverse problems in magnetostatic fields and its application to a source position searching of the human eye fields *J. Appl. Phys.* **67** 5830–2
- Saito Y and Yoda K 1996 Method of generating energy distribution *Japan. Patent Application* 408315279
- Saotome H, Coulomb J L, Saito Y and Sabonnadiere J C 1995 Magnetic core shape design by the sampled pattern matching method *IEEE Trans. Magn.* **31** 1976–9
- Saotome H, Doi T, Hayano S and Saito Y 1993 Crack identification in metallic materials *IEEE Trans. Magn.* **29** 1861–4
- Tidswell T, Gibson A, Bayford R H and Holder D S 2001a Three-dimensional electrical impedance tomography of human brain activity *NeuroImage* **13** 283–94
- Tidswell T, Gibson A, Bayford R H and Holder D S 2001b Validation of a 3D reconstruction algorithm for EIT of human brain function in a realistic head-shaped tank *Physiol. Meas.* **22** 177–85
- Wilson A J, Milnes P, Waterworth A R, Smallwood R H and Brown B H 2001 MK3.5 A modular, multifrequency successor to the M3a EIS/EIT system *Physiol. Meas.* **22** 49–54
- Xie Y Q, Yuan J S, Ma X S and Guan X 2001 Calculation of EEG problems with anisotropic conducting media by the finite volume method *IEEE Trans. Magn.* **37** 3749–52
- Yerworth R J, Bayford R H, Cusick G, Conway M and Holder D S 2002 Design and performance of the UCLH Mark 1b 64 channel electrical impedance tomography (EIT) system, optimized for imaging brain function *Physiol. Meas.* **23** 149–58
- Yoda K, Saito Y and Sakamoto H 1997 Dose optimization of proton and heavy ion therapy using generalized sampled pattern matching *Phys. Med. Biol.* **42** 2411–20
- Yorkey T J, Webster J G and Tompkins W J 1987 Comparing reconstruction algorithms for electrical impedance tomography *IEEE Trans. Biomed. Eng.* **34** 843–52